initially aligned with this direction emitted pure circularly polarized photons and remained invariant under scattering. Their superpositions, on the other hand, became entangled with the scattered photon polarization. States that are invariant under coupling to the environment are of interest, not only because of their importance in the quantum measurement process but also because of their potential use for quantum control purposes. Invariant states can span decoherence-free subspaces in which quantum information can be protected (*21*). It would be therefore interesting to search for multi-spin states that are invariant under photon scattering, and detection, by using larger arrays of trapped ions.

References and Notes

1. W. H. Zurek, *Rev. Mod. Phys.* **75**, 715 (2003).
2. This mechanism is different than the process of ein-selection in decoherence theory, in which the mutual interaction between a quantum system, a measurement apparatus, and their environment results in the emergence of a preferred basis (*1*).
3. C. J. Myatt *et al.*, *Nature* **403**, 269 (2000).
4. M. Brune *et al.*, *Phys. Rev. Lett.* **77**, 4887 (1996).
5. M. S. Chapman *et al.*, *Phys. Rev. Lett.* **75**, 3783 (1995).
6. M. Mei, M. Weitz, *Phys. Rev. Lett.* **86**, 559 (2001).
7. D. A. Kokorowski, A. D. Cronin, T. D. Roberts, D. E. Pritchard, *Phys. Rev. Lett.* **86**, 2191 (2001).
8. R. Ozeri *et al.*, *Phys. Rev. Lett.* **95**, 030403 (2005).
9. H. Uys *et al.*, *Phys. Rev. Lett.* **105**, 200401 (2010).
10. N. Akerman, S. Kotler, Y. Glickman, R. Ozeri, *Phys. Rev. Lett.* **109**, 103601 (2012).
11. D. B. Hume, T. Rosenband, D. J. Wineland, *Phys. Rev. Lett.* **99**, 120502 (2007).
12. A. H. Myerson *et al.*, *Phys. Rev. Lett.* **100**, 200502 (2008).
13. A. Keselman, Y. Glickman, N. Akerman, S. Kotler, R. Ozeri, *New J. Phys.* **13**, 073027 (2011).
14. B. B. Blinov, D. L. Moehring, L. M. Duan, C. Monroe, *Nature* **428**, 153 (2004).
15. J. Volz *et al.*, *Phys. Rev. Lett.* **96**, 030404 (2006).
16. N. Akerman, S. Kotler, Y. Glickman, A. Keselman, R. Ozeri, *App. Phys. B*, 10.1007/s00340-011-4807-6 (2011).
17. Materials and methods are available as supplementary materials on *Science* Online.
18. Cohen-Tannoudji, Claude and Diu, Bernard and Laloe, Frank, *Quantum Mechanics* (Wiley-Interscience 2006), Vol. 2, p. 1048.
19. M. A. Nielsen, I. L. Chuang, *Quantum Computation and Quantum Information* (Cambridge Univ. Press, Cambridge, 2000).
20. M. B. Plenio, S. Virmani, *Quant. Inf. Comput.* **7**, 1 (2007).
21. D. A. Lidar, I. L. Chuang, K. B. Whaly, *Phys. Rev. Lett.* **81**, 2594 (1998).

Acknowledgments: Y.G. and S.K. have equally contributed to this work. We thank N. Davidsson and D. Stamper-Kurn for useful comments on the manuscript. We gratefully acknowledge the support by the Israeli Science Foundation, the Minerva Foundation, the German-Israeli Foundation for scientific research, the Crown Photonics Center, and M. Kushner Schnur, Mexico.

Supplementary Materials

www.sciencemag.org/cgi/content/full/339/6124/1187/DC1
Materials and Methods
Figs. S1 to S4

3 September 2012; accepted 2 January 2013
10.1126/science.1229650

A Transforming Metal Nanocomposite with Large Elastic Strain, Low Modulus, and High Strength

Shijie Hao,[1] Lishan Cui,[1]* Daqiang Jiang,[1] Xiaodong Han,[2]* Yang Ren,[3]* Jiang Jiang,[1] Yinong Liu,[4] Zhenyang Liu,[1] Shengcheng Mao,[2] Yandong Wang,[5] Yan Li,[6] Xiaobing Ren,[7,8] Xiangdong Ding,[7] Shan Wang,[1] Cun Yu,[1] Xiaobin Shi,[1] Minshu Du,[1] Feng Yang,[1] Yanjun Zheng,[1] Ze Zhang,[2,9] Xiaodong Li,[10] Dennis E. Brown,[11] Ju Li[7,12]*

Freestanding nanowires have ultrahigh elastic strain limits (4 to 7%) and yield strengths, but exploiting their intrinsic mechanical properties in bulk composites has proven to be difficult. We exploited the intrinsic mechanical properties of nanowires in a phase-transforming matrix based on the concept of elastic and transformation strain matching. By engineering the microstructure and residual stress to couple the true elasticity of Nb nanowires with the pseudoelasticity of a NiTi shape-memory alloy, we developed an in situ composite that possesses a large quasi-linear elastic strain of over 6%, a low Young's modulus of ~28 gigapascals, and a high yield strength of ~1.65 gigapascals. Our elastic strain-matching approach allows the exceptional mechanical properties of nanowires to be exploited in bulk materials.

It is challenging to develop bulk materials that exhibit a large elastic strain, a low Young's modulus, and a high strength because of the intrinsic trade-off relationships among these properties (*1*, *2*). A low Young's modulus in a single-phase material usually means weak interatomic bonding and thus low strength. Because of the initiation of dislocation activity and/or early failure caused by structural flaws, the elastic strain of bulk metals is usually limited to less than 1%. Because freestanding nanowires have ultrahigh elastic strain limits (4 to 7%) and yield strengths (*3*–*9*), it is expected that composites made with nanowires will have exceptional mechanical properties. However, the results obtained so far have been disappointing (*10*), primarily because the intrinsic mechanical properties of nanowires have not been successfully exploited in bulk composites (*10*–*12*). A typical example is the Nb nanowire–Cu matrix composite, in which the nanowires are well dispersed and well aligned, with strong interfacial bonding. The elastic strain limit achieved in the Nb nanowires in this type of composite is only ~1.5% (*13*, *14*), far below what may be expected of freestanding nanowires (*3*–*9*).

To optimize the retention of nanowire properties in a composite, we hypothesize that the matrix should not deform via sharp microscopic defects such as cracks or dislocations but rather should be rubbery or gluelike, which suggests the use of a shape-memory alloy (SMA) as the matrix. There are two main differences between an SMA matrix and a conventional, plastically deforming metal matrix. First, macroscopically, SMA supports a large pseudoelastic strain of ~7% by stress-induced martensitic transformation (SIMT) (*15*, *16*), which is a strain magnitude comparable to nanowire elasticity (*3*–*9*). Use of an SMA as the matrix allows one to match the high pseudoelasticity of the SMA with the high elasticity of nanowires, as illustrated in Fig. 1A. Second, SIMT and dislocation slip are fundamentally different processes at the atomic scale. Whereas the inelastic shear strain between two adjacent atomic planes approaches 100% after dislocation slip (*17*), the atomic-level inelastic or transformation strain is ~10% after SIMT in typical SMAs such as NiTi (*16*). Therefore, inelastic strain incompatibilities (which must be compensated for by the elastic strain field to maintain cohesion) are much milder at the SMA-nanowire interface than at typical dislocation–piled-up interfaces.

To verify this hypothesis, we selected Nb nanowires to be combined with a NiTi SMA. The NiTi-Nb system with ~20 atomic % Nb undergoes eutectic solidification into a microstructure consisting of fine Nb lamellae (*18*), which can be converted into Nb nanowires through severe plastic deformation. In this study, an ingot with a composition of $Ni_{41}Ti_{39}Nb_{20}$ (atomic %) was prepared by means of vacuum induction

[1]State Key Laboratory of Heavy Oil Processing, China University of Petroleum, Beijing 102249, China. [2]Institute of Microstructure and Properties of Advanced Materials, Beijing University of Technology, Beijing 100124, China. [3]X-ray Science Division, Argonne National Laboratory, Argonne, IL 60439, USA. [4]School of Mechanical and Chemical Engineering, The University of Western Australia, Crawley, WA 6009, Australia. [5]State Key Laboratory for Advanced Metals and Materials, University of Science and Technology Beijing, Beijing 100083, China. [6]School of Materials Science and Engineering, Beihang University, Beijing 100191, China. [7]State Key Laboratory for Mechanical Behavior of Materials and Frontier Institute of Science and Technology, Xi'an Jiaotong University, Xi'an 710049, China. [8]Ferroic Physics Group, National Institute for Materials Science, Tsukuba, 305-0047 Ibaraki, Japan. [9]State Key Laboratory of Silicon Materials, Zhejiang University, Hangzhou 310058, China. [10]Department of Mechanical Engineering, University of South Carolina, Columbia, SC 29208, USA. [11]Department of Physics, Northern Illinois University, De Kalb, IL 60115, USA. [12]Department of Nuclear Science and Engineering and Department of Materials Science and Engineering, Massachusetts Institute of Technology, Cambridge, MA 02139, USA.

*To whom correspondence should be addressed. E-mail: lishancui63@126.com (L.C.); xdhan@bjut.edu.cn (X.H.); ren@aps.anl.gov (Y.R.); liju@mit.edu (J.L.)

melting (fig. S1). Macroscopic wires of the in situ composite (nanowire in situ composite with SMA, hereinafter referred to as NICSMA) with diameters of 0.3 to 1.0 mm were subsequently fabricated by forging, wire-drawing, and annealing (Fig. 1B) (*19*). The typical microstructure of NICSMA (Fig. 1, C to E) consists of Nb nanowires formed in situ with a mean diameter of 60 nm, well dispersed and well aligned in the NiTi matrix along the wire axial direction, with well-bonded interfaces. The selected-area electron diffraction (SAED) pattern (Fig. 1F) is indexed to body-centered cubic Nb and B2-NiTi phases. The phase components of the composite were further characterized by high-energy x-ray diffraction (HE-XRD) (fig. S2) and energy-dispersive x-ray spectroscopic analysis (fig. S3). Both SAED and HE-XRD demonstrate that the Nb nanowires are well oriented with its [110] direction parallel to the wire axial direction. Figure 1, G and H, shows the morphologies of freestanding Nb nanowires obtained by removing the NiTi matrix via electrolytic etching (fig. S4), revealing that the Nb nanowires have lengths ranging from 1 to 100 μm and a mean aspect ratio exceeding 100.

In situ synchrotron HE-XRD (fig. S5) was carried out on NICSMA at room temperature. The evolution of the diffraction peaks for B2-NiTi (211) and B19′-NiTi (001) (fig. S6) indicates that the NiTi matrix underwent an elastic deformation followed by SIMT during tensile loading. Figure 2A shows the evolution of *d*-spacing strain with respect to the applied macroscopic strain for the Nb (220) plane perpendicular to the loading direction, illustrating that the Nb nanowires exhibited a tensile elastic strain of 4.2% when embedded in the SIMT matrix. This elastic strain limit of the Nb nanowires is comparable to that of freestanding nanowires (*3*–*9*). Furthermore, the elastic strain limits of the nanowires embedded in the SIMT matrix increase gradually with decreasing nanowire diameter. The maximum elastic strain limit of the Nb nanowires observed (fig. S7) was 6.5% (the red curve in Fig. 2A). In contrast, we found that, whenever the NiTi matrix deformed by dislocation slip instead of by SIMT after the initial elastic deformation (fig. S8), the elastic strain limits of the Nb nanowires are greatly reduced to ~1.3% (the black curve in Fig. 2A). Figure 2B shows a comparison of the elastic strain limits of (a) Nb nanowires in the matrix deforming by dislocation slip (*13*, *14*, *20*–*22*), (b) Nb nanowires in the matrix deforming by SIMT, and (c) some freestanding nanowires (*3*–*9*).

After pretreatment with a tensile strain cycle of 9.5%, the bulk NICSMA exhibited a large quasi-linear elastic strain of over 6%, a low Young's modulus of ~28 GPa, and a high yield strength of minimum 1.65 GPa within the temperature range of 15° to 50°C (Fig. 3, A and B). In comparison with other known bulk metals with low Young's moduli—for example, Mg, Al, and Ti alloys and gum metals (*1*, *2*, *23*, *24*)—the yield strength of NICSMA is superior. Figure 3, C and D, shows general comparisons of the elastic strain limit, Young's modulus, and yield strength of NICSMA and other metals (*1*, *2*, *23*–*25*) and human bones (*23*). NICSMA occupies a unique spot on a chart of the mechanical properties of various bulk materials (fig. S9) and possesses good cytocompatibility (figs. S10 and S11) and corrosion resistance in a physiological environment (fig. S12).

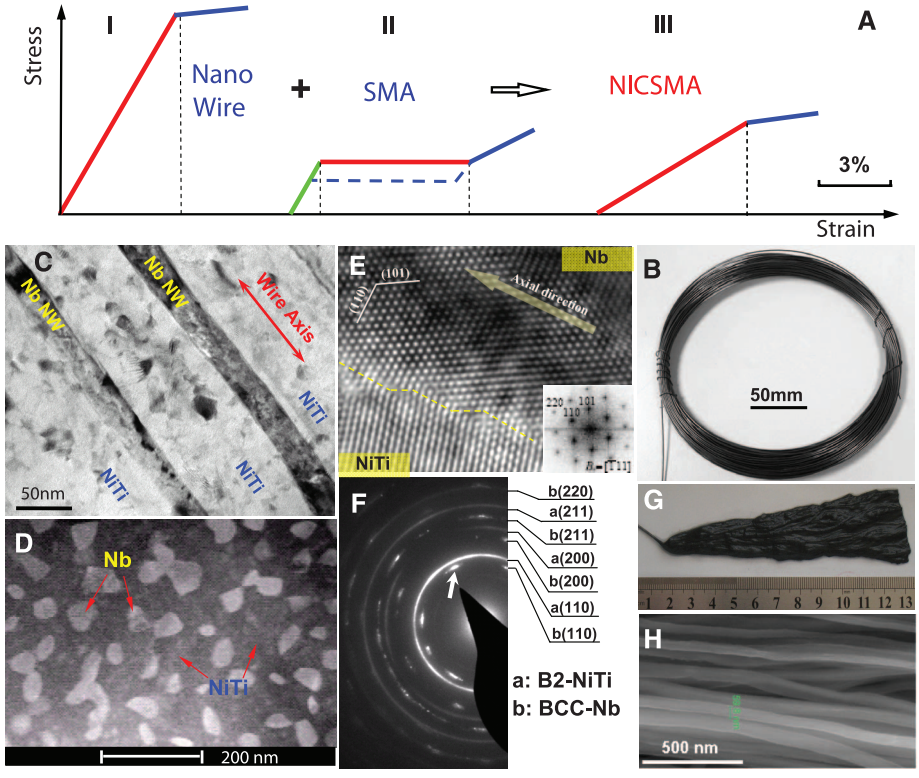

Fig. 1. (**A**) Schematic of the design concept of NICSMA. Schematic tensile stress-strain curves of a high-strength metallic nanowire (I), an SMA (II), and a NICSMA (III). (**B**) A coil of NICSMA wire with a diameter of 0.5 mm. (**C**) Transmission electron microscopy (TEM) image of a longitudinal section of NICSMA wire. NW indicates nanowire. (**D**) Scanning TEM image of the cross section of NICSMA wire (bright regions, cross sections of Nb nanowires; dark regions, NiTi matrix). (**E**) High-resolution TEM image of the interface between the Nb nanowire and the NiTi matrix. (**F**) SAED pattern from a longitudinal section of NICSMA wire. (**G**) Macroscopic appearance of a bundle of freestanding Nb nanowires. (**H**) Scanning electron microscopy image of the freestanding Nb nanowires.

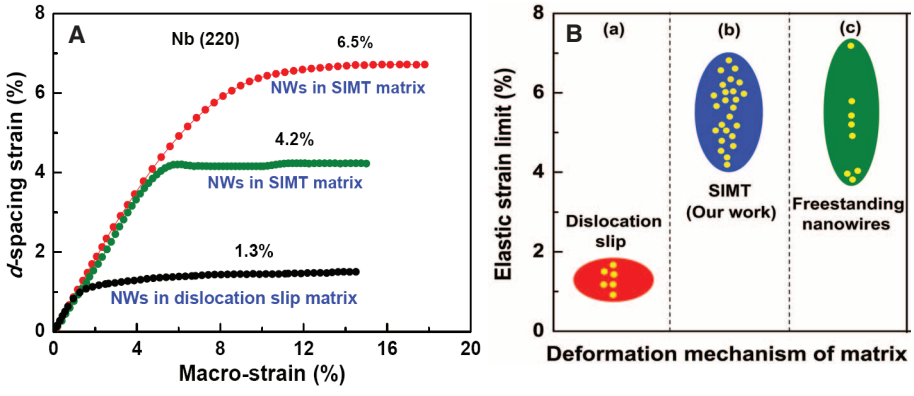

Fig. 2. Elastic strain limits of nanowires. (**A**) Evolution of the *d*-spacing strain with respect to the applied macroscopic strain for the Nb (220) plane perpendicular to the loading direction in the NICSMA wires in which the NiTi matrix deformed by SIMT and dislocation slip. The green curve (with a maximum strain of 4.2%) corresponds to the sample shown in Fig. 1 with 60-nm-diameter Nb nanowires. The red curve (with a maximum strain of 6.5%) corresponds to a different sample (fig. S7), with even narrower Nb nanowires. (**B**) Comparison of the elastic strain limits of (a) Nb nanowires embedded in the matrix deforming by dislocation slip (*13*, *14*, *20*–*22*), (b) Nb nanowires embedded in the matrix deforming by SIMT, and (c) some freestanding nanowires (*3*–*9*).

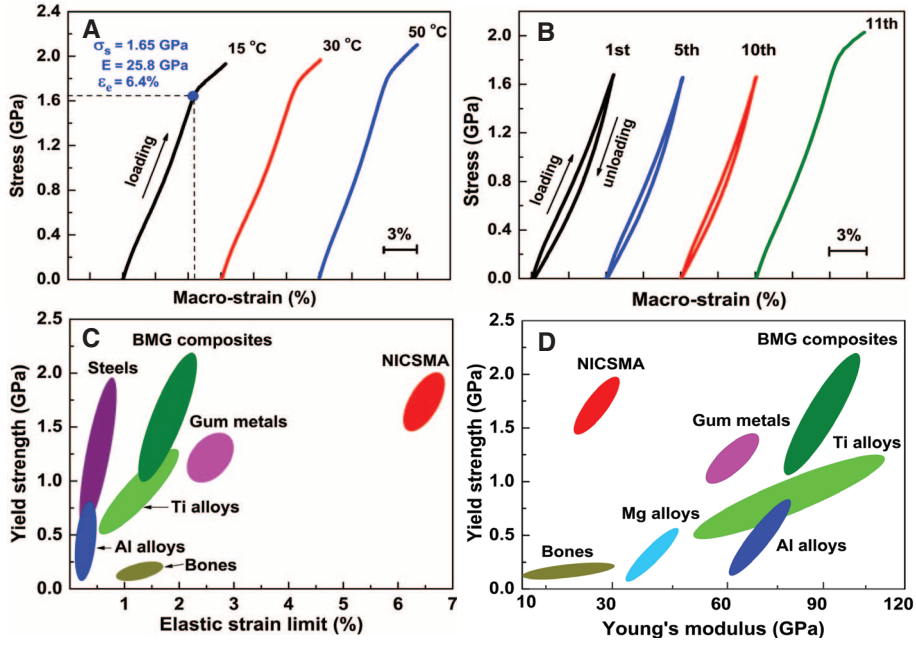

Fig. 3. Typical macroscopic mechanical properties of NICSMA. (**A**) Tensile stress-strain curves of a pretreated NICSMA at 15°, 30°, and 50°C. σ_S, yield strength; E, Young's modulus; ε_e, elastic strain limit. (**B**) Cyclic tensile stress-strain curves of a pretreated NICSMA at room temperature. (**C**) Comparison of the yield strengths and elastic strain limits of different materials. (**D**) Comparison of the yield strengths and Young's moduli of different materials.

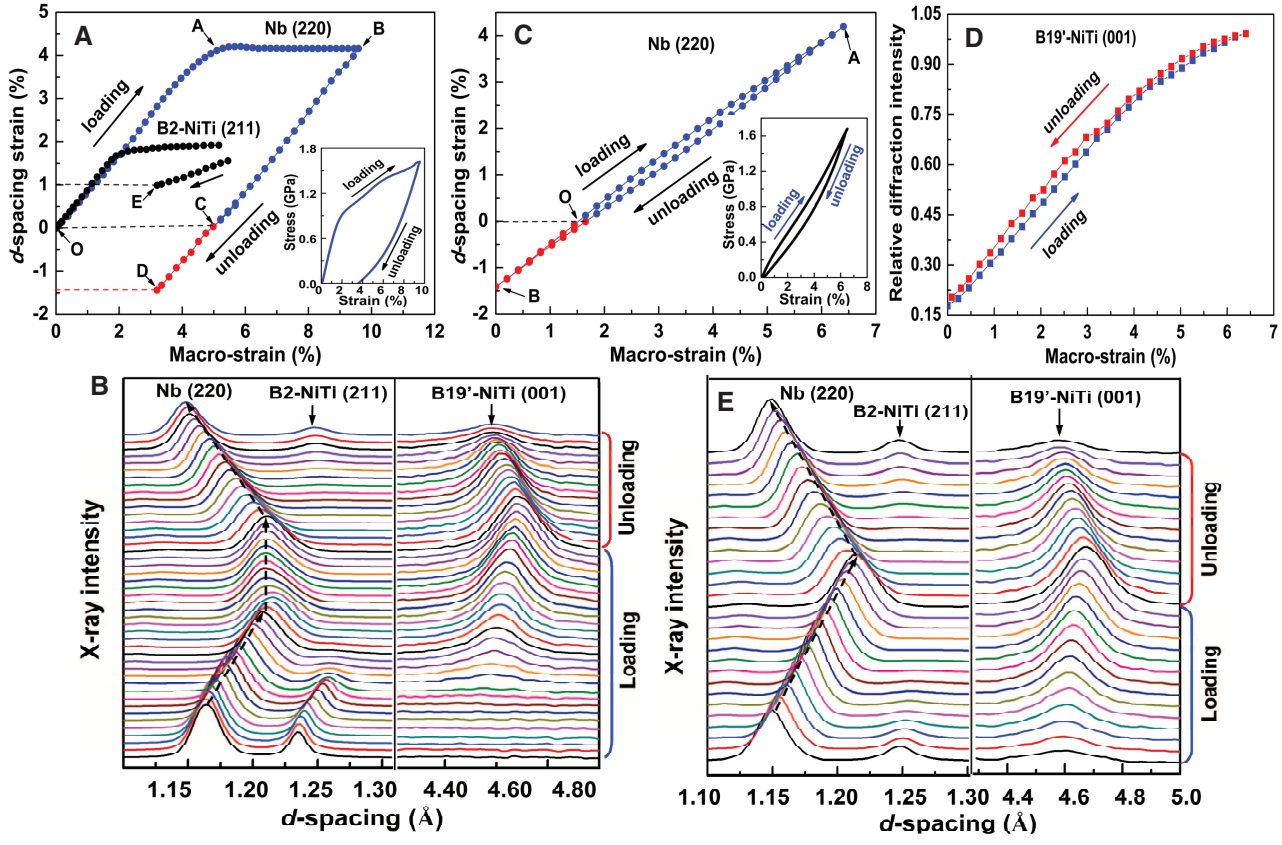

Fig. 4. Microscopic responses of NICSMA revealed by in situ synchrotron HE-XRD. (**A**) Evolution of the *d*-spacing strain for Nb (220) and B2-NiTi (211) planes perpendicular to the loading direction during the pretreatment. (Inset) The macroscopic stress-strain curve of the pretreatment. (**B**) Evolution of the diffraction peaks of Nb (220), B2-NiTi (211), and B19′-NiTi (001) during the pretreatment. (**C**) Evolution of the *d*-spacing strain for Nb (220) plane perpendicular to the loading direction during the subsequent tensile cycle. (Inset) The cyclic stress-strain curve. (**D**) Evolution of the relative intensity of the B19′-NiTi (001) diffraction peak during the subsequent tensile cycle. The relative intensity is defined as the ratio of the integrated area of the B19′-NiTi (001) diffraction peak at a given applied strain to that of the B19′-NiTi (001) diffraction peak at the maximum applied strain. (**E**) Evolution of the diffraction peaks of Nb (220), B2-NiTi (211), and B19′-NiTi (001) during the subsequent tensile cycle. The B2-versus-B19′ peak intensity changes continuously, indicating continuous SIMT throughout the tensile loading.

In situ synchrotron HE-XRD was used to characterize the deformation and phase transformation evolutions of the Nb nanowires and the NiTi matrix, during the pretreatment (Fig. 4A, inset) and the subsequent tensile cycle (Fig. 4C, inset). After the pretreatment, the Nb nanowires sustained an elastic compressive strain of –1.4% (point D), whereas the NiTi matrix sustained an elastic tensile strain of 1% (point E) (Fig. 4A). There is also some retained B19′ phase in the matrix (Fig. 4B). These results can be understood as follows. Upon removal of the pretreatment load, the plastically deformed Nb nanowires (A to B in Fig. 4A) hindered the recovery of the NiTi matrix because of the B19′→B2 transformation (*15*, *16*), which caused large residual strains in the nanowires and the SMA with some retained B19′ phase. This demonstrates that strong coupling between the nanowires and the matrix took place during the pretreatment. In the subsequent tensile cycle (Fig. 4C), the elastic strain achieved in the Nb nanowires was up to 5.6% (A to B), consisting of the preexisting elastic compressive strain of –1.4% (O to B) and an elastic tensile strain of 4.2% (O to A). The NiTi matrix went through continuous SIMT throughout the tensile loading and exhibited an ultralow tangential effective modulus (Fig. 4, D and E) rather than undergoing an initial elastic deformation followed by an abrupt SIMT transition, as would occur in a monolithic SMA (*16*). The continuous SIMT can be ascribed to the contribution of the preexisting internal tensile stress and the retained B19′ phase in the matrix. Upon unloading, the NiTi matrix underwent a reverse transformation from the stress-induced martensite to the parent phase (Fig. 4, D and E), introducing a small hysteresis in the stress-strain curve resulting from energy dissipation during the process. The experimental evidence presented above demonstrates that the Nb nanowires experienced an ultrawide elastic strain of 4.2% – (–1.4%) = 5.6%, which closely matches the phase transformation strain of ~7% of NiTi. This matching of elastic and transformation strains results in the extraordinary properties of NICSMA.

References and Notes

1. M. F. Ashby, *Materials Selection in Mechanical Design* (Butterworth-Heinemann, Burlington, VT, 2005).
2. T. Saito *et al*., *Science* **300**, 464 (2003).
3. E. W. Wong, P. E. Sheehan, C. M. Lieber, *Science* **277**, 1971 (1997).
4. T. Zhu, J. Li, *Prog. Mater. Sci.* **55**, 710 (2010).
5. Y. Yue, P. Liu, Z. Zhang, X. Han, E. Ma, *Nano Lett.* **11**, 3151 (2011).
6. G. Richter *et al*., *Nano Lett.* **9**, 3048 (2009).
7. L. Tian *et al*., *Nat Commun.* **3**, 609 (2012).
8. K. Koziol *et al*., *Science* **318**, 1892 (2007).
9. D. A. Walters *et al*., *Appl. Phys. Lett.* **74**, 3803 (1999).
10. Y. Dzenis, *Science* **319**, 419 (2008).
11. P. Podsiadlo *et al*., *Science* **318**, 80 (2007).
12. J. N. Coleman, U. Khan, Y. K. Gun'ko, *Adv. Mater.* **18**, 689 (2006).
13. L. Thilly *et al*., *Acta Mater.* **57**, 3157 (2009).
14. V. Vidal *et al*., *Scr. Mater.* **60**, 171 (2009).
15. K. Otsuka, C. M. Wayman, Eds., *Shape Memory Materials* (Cambridge Univ. Press, Cambridge, 1998).
16. K. Otsuka, X. Ren, *Prog. Mater. Sci.* **50**, 511 (2005).
17. S. Ogata, J. Li, S. Yip, *Science* **298**, 807 (2002).
18. M. Piao, S. Miyazaki, K. Otsuka, *Mater. Trans. Jpn. Inst. Met.* **33**, 337 (1992).
19. See supplementary materials on *Science* Online.
20. C. C. Aydıner, D. W. Brown, N. A. Mara, J. Almer, A. Misra, *Appl. Phys. Lett.* **94**, 031906 (2009).
21. L. Thilly *et al*., *Appl. Phys. Lett.* **88**, 191906 (2006).
22. C. Scheuerlein, U. Stuhr, L. Thilly, *Appl. Phys. Lett.* **91**, 042503 (2007).
23. M. Niinomi, M. Nakai, *Int. J. Biomater.* **2011**, 1 (2011).
24. M. Niinomi, *Metall. Mater. Trans. A Phys. Metall. Mater. Sci.* **33**, 477 (2002).
25. D. C. Hofmann *et al*., *Nature* **451**, 1085 (2008).

Acknowledgments: We thank G. H. Wu, H. B. Xu, and Y. F. Zheng for valuable discussions on the deformation mechanism of NICSMA. This work is supported by the key program project of National Natural Science Foundation of China (NSFC) (51231008), the National 973 programs of China (2012CB619400 and 2009CB623700), and the NSFC (51071175, 51001119, 50831001, and 10825419). J.L. also acknowledges support by NSF DMR-1008104 and DMR-1120901. X.D.H. acknowledges support by the Beijing High-level Talents (PHR20100503), the Beijing PXM201101420409000053, and Beijing 211 project. D.E.B. acknowledges support by the Institute for NanoScience, Engineering, and Technology (INSET) of Northern Illinois University. Use of the Advanced Photon Source was supported by the U.S. Department of Energy, Office of Science, under contract no. DE-AC02-06CH11357.

Supplementary Materials

www.sciencemag.org/cgi/content/full/339/6124/1191/DC1
Materials and Methods
Figs. S1 to S12
References (*26*–*30*)

9 August 2012; accepted 10 January 2013
10.1126/science.1228602

Terrestrial Accretion Under Oxidizing Conditions

Julien Siebert,[1]* James Badro,[2] Daniele Antonangeli,[1] Frederick J. Ryerson[2,3]

The abundance of siderophile elements in the mantle preserves the signature of core formation. On the basis of partitioning experiments at high pressure (35 to 74 gigapascals) and high temperature (3100 to 4400 kelvin), we demonstrate that depletions of slightly siderophile elements (vanadium and chromium), as well as moderately siderophile elements (nickel and cobalt), can be produced by core formation under more oxidizing conditions than previously proposed. Enhanced solubility of oxygen in the metal perturbs the metal-silicate partitioning of vanadium and chromium, precluding extrapolation of previous results. We propose that Earth accreted from materials as oxidized as ordinary or carbonaceous chondrites. Transfer of oxygen from the mantle to the core provides a mechanism to reduce the initial magma ocean redox state to that of the present-day mantle, reconciling the observed mantle vanadium and chromium concentrations with geophysical constraints on light elements in the core.

The depletion of siderophile (i.e., "iron-loving") elements in Earth's mantle relative to chondrites can constrain the redox state of accreting materials during terrestrial accretion and core differentiation (*1*–*4*). For example, metal-silicate partitioning experiments at atmospheric pressure indicate that the observed depletion of slightly siderophile elements (SSEs) such as V and Cr can only be produced at conditions more reducing than those required to account for the abundance of moderately siderophile elements (such as Ni, Co, and W) or highly siderophile elements (*5*). Using metal-silicate partition coefficients obtained at pressures up to 25 GPa, homogeneous accretion models posit that metal-silicate equilibrium took place at the base of a deep terrestrial magma ocean at a single oxygen fugacity (fO_2) (*6*–*8*). However, the pressure-temperature (*P*-*T*) conditions required to produce the observed depletions for V and Cr (at the present-day fO_2) require temperatures that greatly exceed that of the mantle liquidus (*2*, *4*, *9*, *10*). Such conditions are physically inconsistent with the magma ocean hypothesis, where the *P*-*T* conditions at the base of a magma ocean necessarily lie between the mantle solidus and liquidus, thereby creating a rheological boundary that enables the metal to pond and equilibrate with the silicate melt.

To satisfy this rheological constraint and SSE abundance patterns, recent models of core formation constrain metal-silicate equilibration to the *P*-*T* conditions of the peridotite liquidus and invoke early accretion of highly reduced materials with a FeO-poor silicate component (*2*, *4*, *10*, *11*). These initially low fO_2 conditions (~IW-4, corresponding to 4 log fO_2 units below the iron-wüstite buffer) enhance the siderophile character of the SSEs at the relevant *P*-*T* conditions. Subsequent, gradual oxidation of the mantle to ~IW-2 over the course of core formation is required to account for moderately siderophile element abundances and, most important, to reach the current mantle FeO content [8 weight percent (wt %) FeO in silicate]. Under reducing conditions, silicon is likely to be the only light element entering the core in large amounts (*10*–*12*). This scenario relies on extensive pressure and temperature extrapolation of SSE partitioning data, as existing results are restricted to rela-

[1]Institut de Minéralogie et de Physique des Milieux Condensés, Université Pierre et Marie Curie, UMR CNRS 7590, Institut de Physique du Globe de Paris, 75005 Paris, France. [2]Institut de Physique du Globe de Paris, Université Paris Diderot, 75005 Paris, France. [3]Lawrence Livermore National Laboratory, Livermore, CA 94551, USA.

*To whom correspondence should be addressed. E-mail: julien.siebert@impmc.upmc.fr

www.sciencemag.org/cgi/content/full/339/6124/1191/DC1

Supplementary Materials for

A Transforming Metal Nanocomposite with Large Elastic Strain, Low Modulus, and High Strength

Shijie Hao, Lishan Cui,* Daqiang Jiang, Xiaodong Han,* Yang Ren,* Jiang Jiang, Yinong Liu, Zhenyang Liu, Shengcheng Mao, Yandong Wang, Yan Li, Xiaobing Ren, Xiangdong Ding, Shan Wang, Cun Yu, Xiaobin Shi, Minshu Du, Feng Yang, Yanjun Zheng, Ze Zhang, Xiaodong Li, Dennis E. Brown, Ju Li*

*To whom correspondence should be addressed. E-mail: lishancui63@126.com (L.C.); xdhan@bjut.edu.cn (X.H.); ren@aps.anl.gov (Y.R.); liju@mit.edu (J.L.)

Published 8 March 2013, *Science* **339**, 1191 (2013)
DOI: 10.1126/science.1228602

This PDF file includes:

Materials and Methods

An alloy ingot of 100 mm in diameter and 7 kg in weight with a composition of $Ni_{41}Ti_{39}Nb_{20}$ (at.%) was prepared by vacuum induction melting. The raw materials used were of commercial purity Ni (99.96 wt.%), Ti (99.90 wt.%) and Nb (99.99 wt.%). The ingot was hot-forged at 850 °C into a rod of 16 mm in diameter and further hot-drawn at 750 °C into a thick wire of 2 mm in diameter. Then the hot-drawn wire was cold-drawn into thin wires of 0.3−1.0 mm in diameter at room temperature with intermediate annealing at 700 °C (Fig. 1B). The test samples were cut from the cold-drawn wires and subsequently annealed at 375 °C for 20 min followed by air cooling.

Some freestanding Nb nanowires were extracted from the cold-drawn wires by chemically removing the NiTi matrix by means of electrolytic etching (Fig. S4). The electrolyte used was a 25% HNO_3 - methanol solution. The etching was conducted at a DC voltage of 4 V with a graphite cathode.

In situ synchrotron high-energy X-ray diffraction measurements were performed at the 11-ID-C beamline of the Advanced Photon Source at Argonne National Laboratory. High-energy X-rays of 114.76 keV energy and 0.6 mm × 0.6 mm beam size were used to obtain two-dimensional (2D) diffraction patterns in the transmission geometry using a Perkin-Elmer large area detector placed downstream at 1.6 m away from the sample (Fig. S5). The 2D diffraction patterns were collected during tensile deformation using a home-made mechanical testing device. Gaussian fits were used to determine diffraction peak

positions and areas. Errors of the *d*-spacing strain measurement and the relative peak intensity measurement are estimated to be smaller than 0.1% and 0.02, respectively. Tensile deformation was performed using an Instron testing machine at a strain rate of 1×10^{-4} s^{-1} and the total elongation of the gauge length was measured with a static axial clip-on extensometer.

Microstructure and chemical composition of NICSMA wire were analyzed using a FEI Tecnai G2 F20 transmission electron microscope equipped with an energy dispersive X-ray spectroscopic analyzer operated at a voltage of 200 kV. The morphology of the freestanding Nb nanowires extracted from NICSMA was characterized using a FEI Quanta 200F scanning electron microscope operated at a voltage of 20 kV.

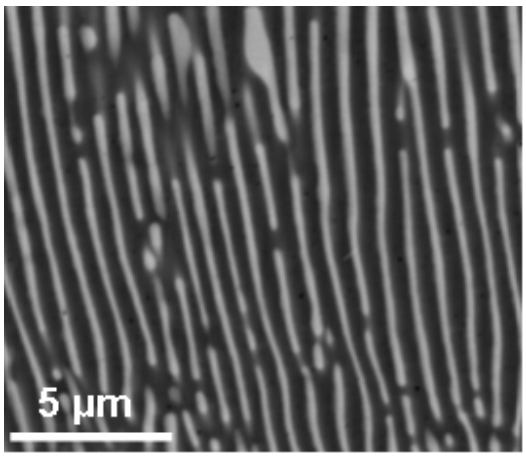

Fig. S1. Scanning electron microscopy (SEM) image of the NiTi-Nb eutectic microstructure in the alloy ingot (bright regions: fine Nb lamellae; dark regions: NiTi matrix).

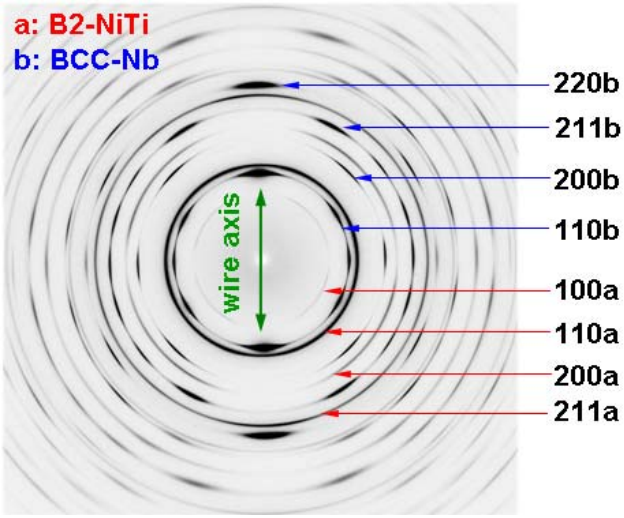

Fig. S2. Two-dimensional high-energy X-ray diffraction (HE-XRD) pattern obtained from the longitudinal-section of a NICSMA wire which was aligned vertically.

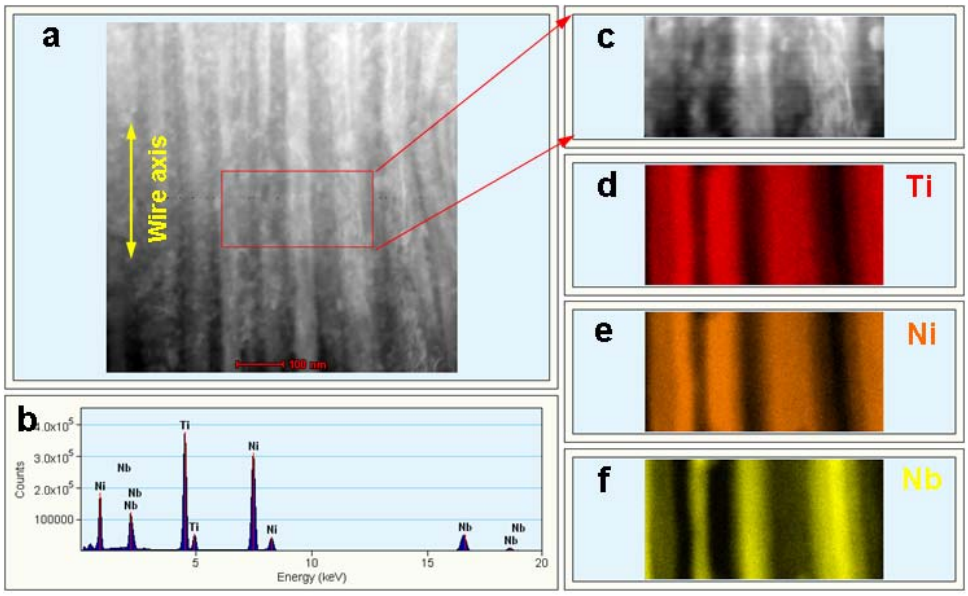

Fig. S3. Energy dispersive X-ray spectroscopy analysis of the chemical composition distribution of a NICSMA sample. (**a**) Low-magnification scanning transmission electron microscopy image of a longitudinal-section of the sample (bright phase: Nb nanowires; dark phase: NiTi matrix). (**b**) Energy dispersive X-ray spectrum of the sample. (**c**) Enlarged view of the region in the red frame in (a). (**d**) Mapping of titanium of the region shown in (c). (**e**) Mapping of nickel of the region shown in (c). (**f**) Mapping of niobium of the region shown in (c). The Nb nanowires contain 80.8 at.% Nb, 16.2 at.% Ti and 3.0 at.% Ni. The NiTi matrix contains 46.2 at.% Ti, 50.7 at.% Ni and 3.1 at.% Nb.

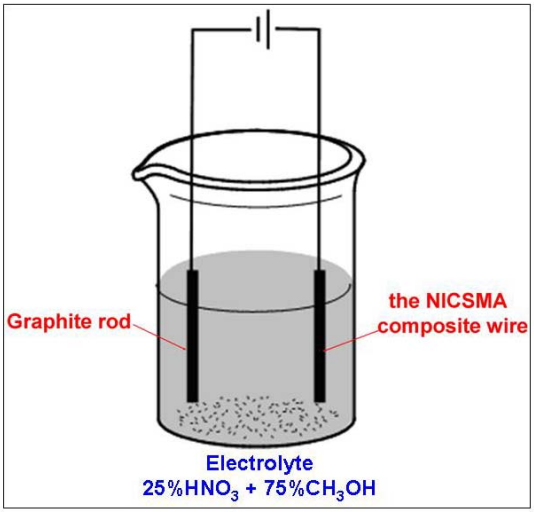

Fig. S4. Schematic illustration of the experimental set-up for the electrolytic extraction of freestanding Nb nanowires from a NICSMA sample.

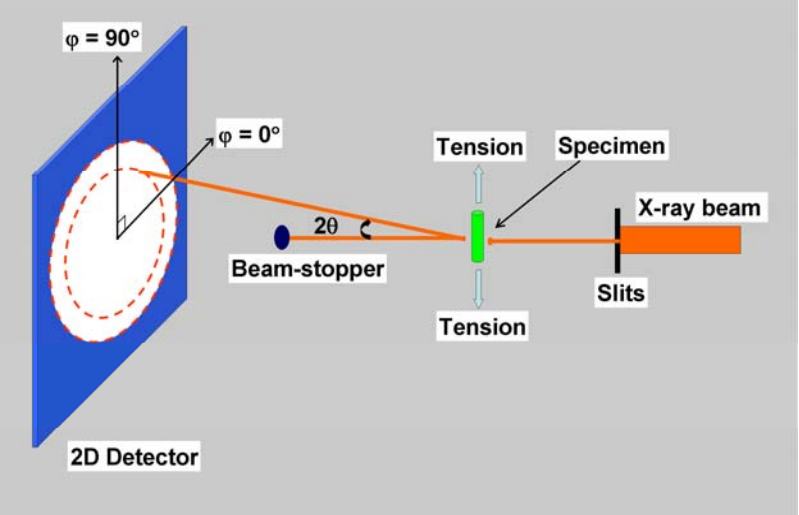

Fig. S5. Schematic illustration of the experimental set-up of in situ synchrotron high-energy X-ray diffraction during tensile testing.

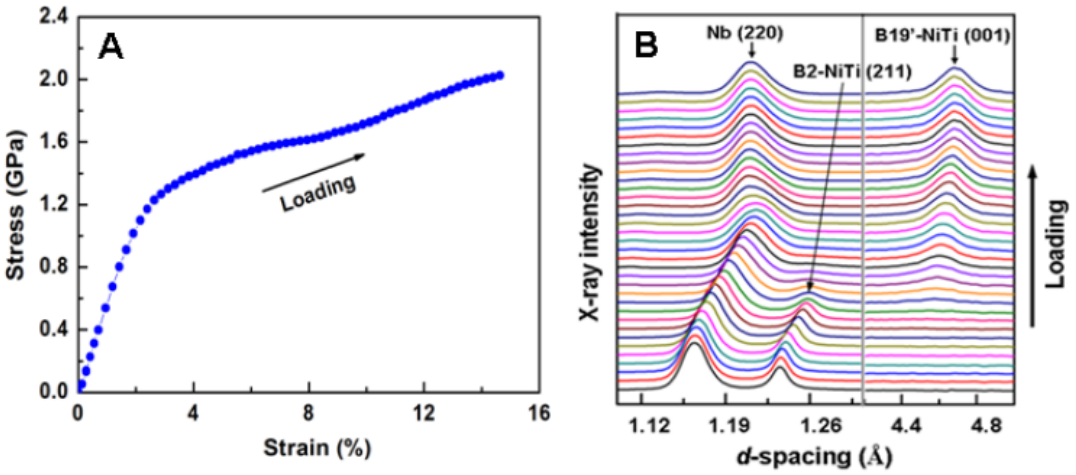

Fig. S6. Tensile stress-strain curve of a NICSMA sample (**A**) and evolutions of the high-energy X-ray diffraction peaks of Nb (220), B2-NiTi (211) and B19'-NiTi (001) obtained during tensile loading at room temperature (**B**).

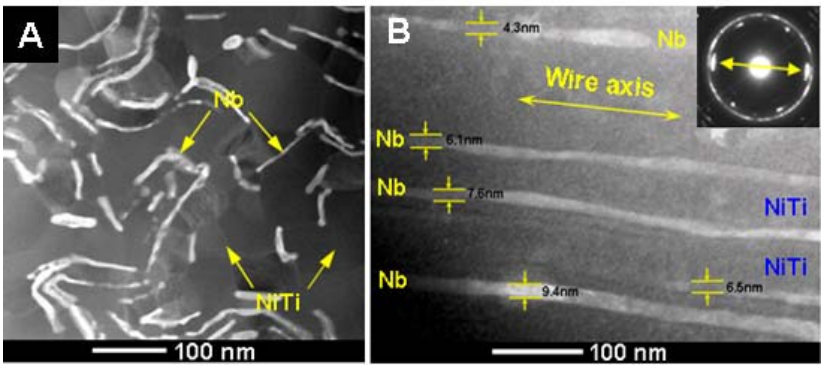

Fig. S7. Scanning transmission electron microscopy images of a cross-section (**A**) and a longitudinal-section (**B**) of a NICSMA wire (bright regions: Nb nanowires; dark regions: NiTi matrix).

Note: The ribbon-shaped Nb nanowires are 3−20 nm in thickness, 20−200 nm in width, and are well dispersed and fully aligned in the NiTi matrix along the wire axial direction.

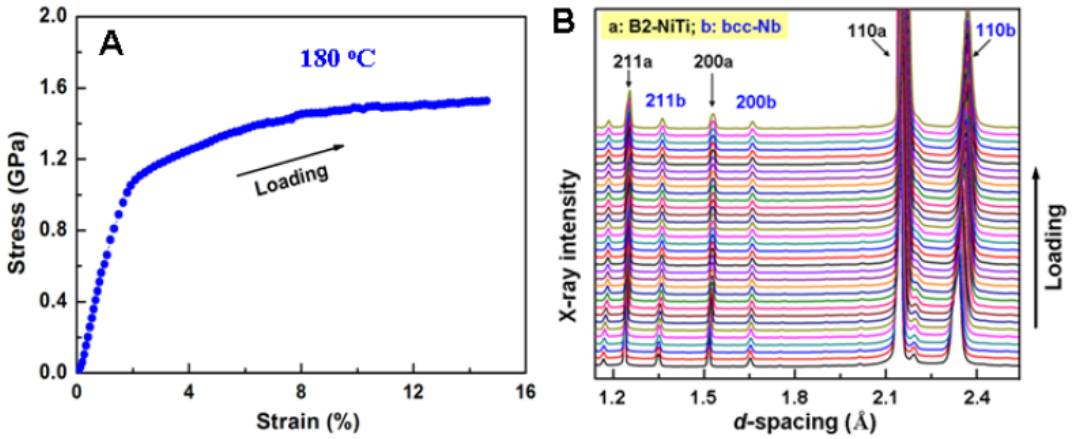

Fig. S8. Tensile stress-strain curve of a NICSMA sample (**A**) and evolutions of the high-energy X-ray diffraction peaks of Nb (220), B2-NiTi (211) and B19'-NiTi (001) during tensile loading at 180 °C (**B**).

Note: It is seen in B that the B2-NiTi matrix survived the entire deformation to 15.5% of global strain without transforming to the B19' martensite at 180°C. This is because the test temperature is higher than the critical temperature at which the critical stress for SIMT equals that for plastic deformation of the austenite (*26*). Through tensile testing of the NISCMA, the critical temperature for SIMT in the NiTi matrix is determined to be ~160 °C, above which dislocation slip occurs as the dominant mechanism of deformation.

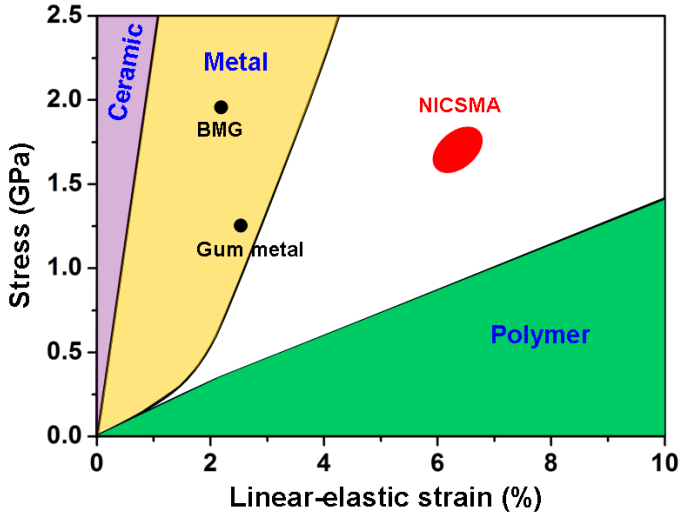

Fig. S9. Comparison of strengths and elastic strains of ceramics, metals, polymers and NICSMA.

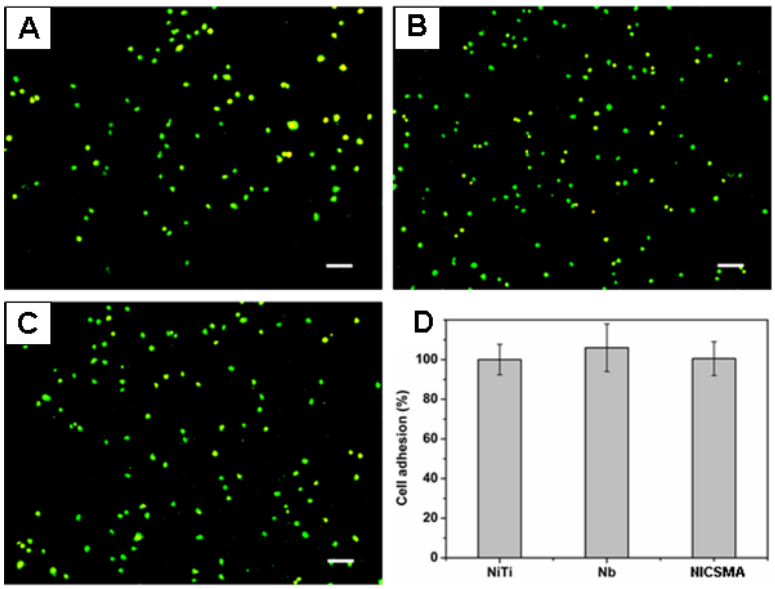

Fig. S10. Cell adhesion of fibroblasts cultured on the surfaces of (**A**) NiTi, (**B**) Nb and (**C**) NICSMA samples. Graph (**D**) shows the statistical cell number after four hours of culture (*$p < 0.05$, mean + SD, N=3). The scale bars at the bottom of the images represent 100 μm.

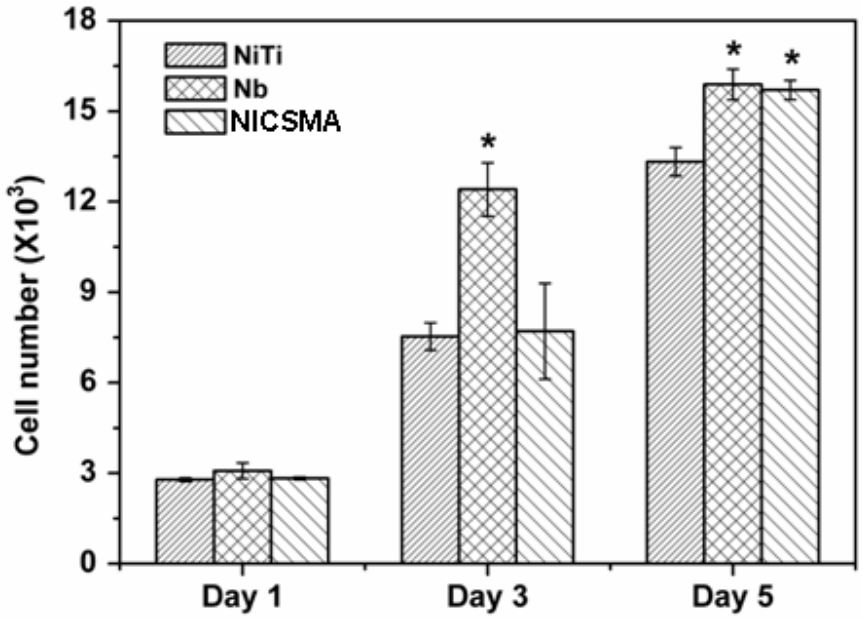

Fig. S11. Methyl-thiazol-tetrazolium (MTT) assay for cell proliferation on NiTi, Nb and NICSMA samples after 1, 3 and 5 days of culture (*$p < 0.05$, mean + SD, N=3).

Note: Nb is one of the most biocompatible metallic elements (*24, 27, 28*) and NiTi has been used in medical treatment in many forms (*29, 30*). From Figs. S10 and S11, it can be concluded that all the samples are well tolerated by fibroblast cells, with Nb and NICSMA samples possessing relatively higher cell proliferation, indicating better cyto-compatibility.

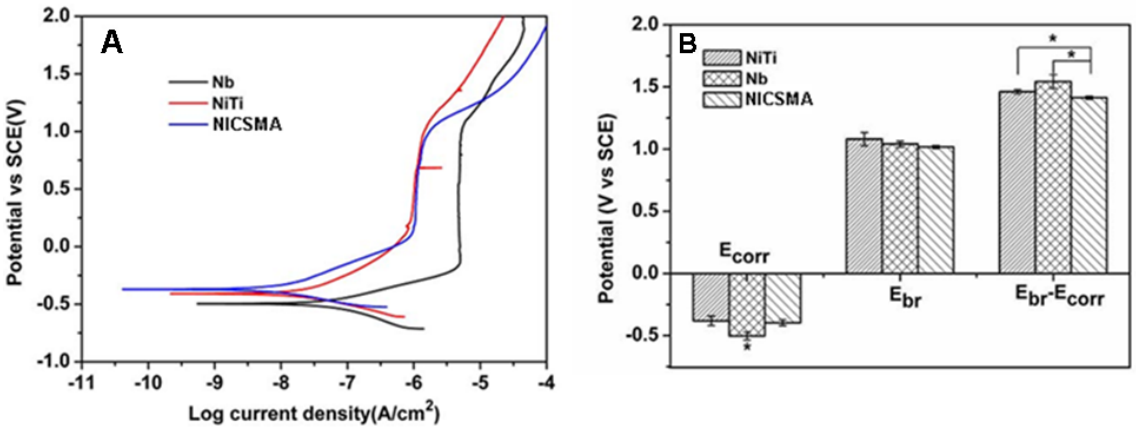

Fig. S12. Electrochemical characteristics of NICSMA. (**A**) Potentiodynamic anodic polarization curves of NICSMA, NiTi and Nb samples in Hanks' solution: 8.00 g/L NaCl, 0.14 g/L CaCl, 0.4 g/L KCl, 0.10 g/L $MgCl_2 \cdot 6H_2O$, 0.10 g/L $MgSO_4 \cdot 7H_2O$, 0.35 g/L $NaHCO_3$, 0.12 g/L $Na_2HPO_4 \cdot 12H_2O$, 0.06 g/L KH_2PO_4 and 1.0 g/L Glucose (pH=7.4) at 310K. (**B**) Statistical analysis of the corrosion potential (E_{corr}), breakdown potential (E_{br}), and (E_{br}-E_{corr}) (*$p < 0.05$, mean± SD, N =3) of the three materials.

References and Notes

1. M. F. Ashby, *Materials Selection in Mechanical Design* (Butterworth-Heinemann, City, 2005).

2. T. Saito *et al*., Multifunctional Alloys Obtained via a Dislocation-Free Plastic Deformation Mechanism. *Science* **300**, 464 (2003). doi:10.1126/science.1081957 Medline

3. E. W. Wong, P. E. Sheehan, C. M. Lieber, Nanobeam Mechanics: Elasticity, Strength, and Toughness of Nanorods and Nanotubes. *Science* **277**, 1971 (1997). doi:10.1126/science.277.5334.1971

4. T. Zhu, J. Li, Ultra-strength materials. *Prog. Mater. Sci.* **55**, 710 (2010). doi:10.1016/j.pmatsci.2010.04.001

5. Y. Yue, P. Liu, Z. Zhang, X. Han, E. Ma, Approaching the theoretical elastic strain limit in copper nanowires. *Nano Lett.* **11**, 3151 (2011). doi:10.1021/nl201233u Medline

6. G. Richter *et al*., Ultrahigh strength single crystalline nanowhiskers grown by physical vapor deposition. *Nano Lett.* **9**, 3048 (2009). doi:10.1021/nl9015107 Medline

7. L. Tian *et al*., Approaching the ideal elastic limit of metallic glasses. *Nat Commun.* **3**, 609 (2012). doi:10.1038/ncomms1619 Medline

8. K. Koziol *et al*., High-performance carbon nanotube fiber. *Science* **318**, 1892 (2007); 10.1126/science.1147635. doi:10.1126/science.1147635 Medline

9. D. A. Walters *et al*., Elastic strain of freely suspended single-wall carbon nanotube ropes. *Appl. Phys. Lett.* **74**, 3803 (1999). doi:10.1063/1.124185

10. Y. Dzenis, Materials science. Structural nanocomposites. *Science* **319**, 419 (2008). doi:10.1126/science.1151434 Medline

11. P. Podsiadlo *et al*., Ultrastrong and stiff layered polymer nanocomposites. *Science* **318**, 80 (2007). doi:10.1126/science.1143176 Medline

12. J. N. Coleman, U. Khan, Y. K. Gun'ko, Mechanical Reinforcement of Polymers Using Carbon Nanotubes. *Adv. Mater.* **18**, 689 (2006). doi:10.1002/adma.200501851

13. L. Thilly *et al*., A new criterion for elasto-plastic transition in nanomaterials: Application to size and composite effects on Cu–Nb nanocomposite wires. *Acta Mater.* **57**, 3157 (2009). doi:10.1016/j.actamat.2009.03.021

14. V. Vidal *et al*., Plasticity of nanostructured Cu–Nb-based wires: Strengthening mechanisms revealed by in situ deformation under neutrons. *Scr. Mater.* **60**, 171 (2009). doi:10.1016/j.scriptamat.2008.09.032

15. K. Otsuka, C. M. Wayman, Eds., *Shape Memory Materials* (Cambridge Univ. Press, Cambridge, 1998).

16. K. Otsuka, X. Ren, Physical metallurgy of Ti–Ni-based shape memory alloys. *Prog. Mater. Sci.* **50**, 511 (2005). doi:10.1016/j.pmatsci.2004.10.001

17. S. Ogata, J. Li, S. Yip, Ideal pure shear strength of aluminum and copper. *Science* **298**, 807 (2002). doi:10.1126/science.1076652 Medline

18. M. Piao, S. Miyazaki, K. Otsuka, *Mater. Trans. Jpn. Inst. Met.* **33**, 337 (1992).

19. See supplementary material on *Science* Online.

20. C. C. Aydıner, D. W. Brown, N. A. Mara, J. Almer, A. Misra, In situ x-ray investigation of freestanding nanoscale Cu–Nb multilayers under tensile load. *Appl. Phys. Lett.* **94**, 031906 (2009). doi:10.1063/1.3074374

21. L. Thilly *et al*., Plasticity of multiscale nanofilamentary Cu⁄Nb composite wires during in situ neutron diffraction: Codeformation and size effect. *Appl. Phys. Lett.* **88**, 191906 (2006). doi:10.1063/1.2202720

22. C. Scheuerleina, U. Stuhr, L. Thilly, In situ neutron diffraction under tensile loading of powder-in-tube Cu⁄Nb[sub 3]Sn composite wires: Effect of reaction heat treatment on texture, internal stress state, and load transfer. *Appl. Phys. Lett.* **91**, 042503 (2007). doi:10.1063/1.2766685

23. M. Niinomi, M. Nakai, Titanium-Based Biomaterials for Preventing Stress Shielding between Implant Devices and Bone. *Int. J. Biomater.* **2011**, 1 (2011). doi:10.1155/2011/836587

24. M. Niinomi, Recent metallic materials for biomedical applications. *Metall. Mater. Trans. A Phys. Metall. Mater. Sci.* **33**, 477 (2002). doi:10.1007/s11661-002-0109-2

25. D. C. Hofmann *et al*., Designing metallic glass matrix composites with high toughness and tensile ductility. *Nature* **451**, 1085 (2008). doi:10.1038/nature06598 Medline

26. Y. Liu, H. Xiang, Apparent modulus of elasticity of near-equiatomic NiTi. *J. Alloy. Comp.* **270**, 154 (1998). doi:10.1016/S0925-8388(98)00500-3

27. H. Matsuno, A. Yokoyama, F. Watari, M. Uo, T. Kawasaki, Biocompatibility and osteogenesis of refractory metal implants, titanium, hafnium, niobium, tantalum and rhenium. *Biomaterials* **22**, 1253 (2001). doi:10.1016/S0142-9612(00)00275-1 Medline

28. E. Eisenbarth, D. Velten, M. Müller, R. Thull, J. Breme, Biocompatibility of beta-stabilizing elements of titanium alloys. *Biomaterials* **25**, 5705 (2004). doi:10.1016/j.biomaterials.2004.01.021 Medline

29. T. Duerig, A. Pelton, D. Stockel, An overview of nitinol medical applications. *Mater. Sci. Eng. A* **273-275**, 149 (1999). doi:10.1016/S0921-5093(99)00294-4

30. D. Stoeckel, Nitinol medical devices and implants. *Minim. Invasive Ther. Allied Technol.* **9**, 81 (2000). doi:10.3109/13645700009063054